Ionic liquid as a template and a carbon source for particle engineering and coating of Na3V2(PO4)2F3-yOy

Gaël Minart, Christine Labrugère-Sarroste, François Weill, Sonia Buffiere, Marie Anne Dourges, Guillaume Clermont, Laurence Croguennec, Jacob Olchowka

Ionic liquid as a template and a carbon source for particle engineering and coating of $Na_3V_2(PO_4)_2F_{3-y}O_y$

Gaël Minart[1,2], Christine Labrugère-Sarroste[4], François Weill[1,2], Sonia Buffière[1], Marie-Anne Dourges[5], Guillaume Clermont[5], Laurence Croguennec[1,2,3], Jacob Olchowka[1,2,3,*]

[1] CNRS, Univ. Bordeaux, Bordeaux INP, ICMCB UMR 5026, F-33600 Pessac, France
[2] RS2E, Réseau Français sur le Stockage Electrochimique de l'Energie, FR CNRS 3459, F-80039 Amiens Cedex 1, France
[3] ALISTORE-ERI European Research Institute, FR CNRS 3104, F-80039 Amiens Cedex 1, France
[4] Univ. Bordeaux, CNRS, PLACAMAT, UAR 3626, F-33600 Pessac, France
[5] Univ. Bordeaux, CNRS, ISM, UMR 5255, F-33400, Talence, France

Abstract

Topochemical synthesis under ionothermal conditions provides a unique pathway for obtaining the polyanionic electrode material $Na_3V_2(PO_4)_2FO_2$ with particles exhibiting a distinctive 2D platelet morphology. This morphology directly originates from the $VOPO_4 \cdot 2H_2O$ precursor through a synthesis process involving water molecules extraction followed by fluorine and sodium insertion in the interlayer space while preserving the overall covalent bond network. This synthesis approach gives the possibility to engineer the active material particles shape through a design of the precursor, while maintaining the same reaction conditions. Herein, three different $VOPO_4 \cdot 2H_2O$ with distinct particle sizes and morphologies were synthetized to evaluate the impact on the resulting $Na_3V_2(PO_4)_2FO_2$ electrochemical performance. The optimal material was sintered under argon flow to transform the ionic liquid-based surface layer into a carbon coating and enhance the active material electronic conductivity. The particles morphology optimization using ionic liquid as templating-agent allowed to improve specific capacity from 56 mAh/g to 83 mAh/g at 1C, while the further carbonization of the ionic liquid surface layer permits to increase active material capacity up to 103 mAh/g, demonstrating the benefits of surface modification.

Keywords: Na-ion batteries, polyanionic electrode material, ionothermal synthesis, coating, surface modification

Email: jacob.olchowka@icmcb.cnrs.fr

1. Introduction:

In recent decades, the growing demand for Li-ion batteries has driven a significant increase in the price of lithium resources, with projections indicating that this trend will continue in the coming years. To address this issue and reduce both costs and environmental impacts, Na-ion batteries have emerged as a viable alternative.[1] These devices are becoming more and more competitive compared to their lithium counterparts, largely due to the fundamental research that led to the development and optimization of various positive electrode materials in recent years.[2–5] Among all of the studied materials, the $Na_3V_2(PO_4)_2F_{3-y}O_y$ ($0 \leq y \leq 2$) family turned out to be one of the most promising candidates thanks to its respectable energy density (~500 Wh/kg), its high ionic conductivity, impressive structural stability upon cycling,[5] good thermal stability and chemical stability to exposure to air and water.[6–10] Within this family of compounds 2 Na^+ per formula unit can be reversibly extracted, however, the highest energy density is obtained for $Na_3V_2(PO_4)_2F_3$, as the fluorine substitution by oxygen tends to lower the working potential. Nevertheless, oxygen-substituted materials offer additional benefits, such as enhanced electrical conductivity and structural stabilization at overcharged states,[11, 12] making them still highly attractive for practical applications.

One of the major drawbacks of these phases is their poor electronic conductivity. In the case of the $Na_3V_2(PO_4)_2F_{3-y}O_y$ ($0 \leq y \leq 2$) materials, the 3D atomic structure consists of $V_2O_{8+y}F_{3-y}$ bi-octahedral units connected by highly covalent phosphate (PO_4) groups, which hinder efficient electronic transfer within the polyanionic framework. Several strategies can help to overcome this issue, such as adjusting particles morphology (nano-sizing, preferential crystallographic orientation)[13–15], engineering the surface chemistry of the material with a carbon coating[16,17] or in a lesser extent modifying the electronic structure through transition metal substitution.[18–20] In practice, a combination of both nanosizing and application of a uniform carbon-coating remains the most promising approach and should be prioritized in further developments, while ensuring that suitable tap density of the electrode material is maintained.[21]

In this work, three different $Na_3V_2(PO_4)_2FO_2$ materials were synthetized using the ionothermal approach previously developed in our group.[22] Ionic liquids are liquid salts at low temperature (< 100°C), with this low melting point primarily resulting from the asymmetry of their cation and/or anion, which hinders crystallization.[23, 24] Their wide temperature range in the liquid state, low vapor pressure and low toxicity make them suitable for the synthesis of inorganic materials. Furthermore, it has been shown in the literature that the presence of an ionic liquid layer at the active material surface can enhance its electrochemical performance.[13,25] The synthesis

mechanism reported in the work of Olchowka *et al.* involved a topochemical reaction that includes the dehydration of a $VOPO_4 \cdot 2H_2O$ precursor followed by the insertion of sodium and fluorine from NaF dissolved in 1-ethyl-3-methylimidazoliumbis(trifluoromethylsulfonyl)imide (EMIM-TFSI) (Figure 1).[22] This topochemical synthesis allowed to preserve precursor's large platelets morphology during the formation of the polyanionic active material. Besides, an ionic liquid coating was found at the particle's surface, enhancing Na^+ conductivity at grain boundaries.[13] Here, three different $Na_3V_2(PO_4)_2FO_2$ materials were synthetized from $VOPO_4 \cdot 2H_2O$ exhibiting various particles size and morphology to tailor the $Na_3V_2(PO_4)_2FO_2$ ones and evaluate the impact on the energy storage performance. Additionally, further annealing experiments were conducted on the best-performing electrode material to transform its ionic liquid-based layer in a carbon coating, with the aim of enhancing its energy storage performance.

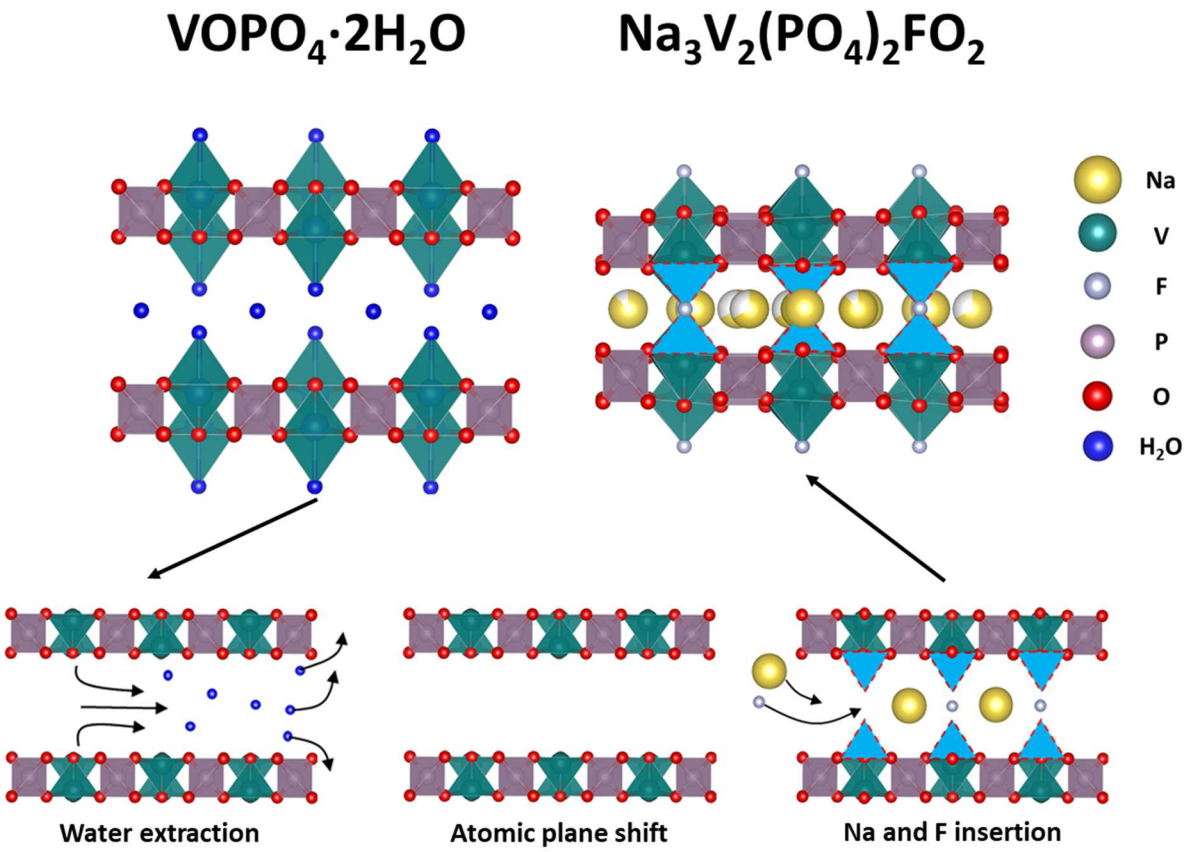

Figure 1: Representation of the topochemical reaction mechanism to synthetize $Na_3V_2(PO_4)_2FO_2$ from $VOPO_4 \cdot 2H_2O$.

2. Experimental section

2.1 $VOPO_4{\cdot}2H_2O$ and $Na_3V_2(PO_4)_2FO_2$ synthesis

Vanadium (V) oxide (V_2O_5, Sigma-Aldrich; ≥ 99.6%) and phosphoric acid (H_3PO_4, Sigma-Aldrich; wt. 85%) were used as the vanadium and phosphate precursors, respectively, to synthetize vanadium phosphate dihydrate ($VOPO_4{\cdot}2H_2O$). Then, the $Na_3V_2(PO_4)_2FO_2$ ($NVPFO_2$) phase was obtained via ionothermal synthesis from a mixture of $VOPO_4{\cdot}2H_2O$ and sodium fluoride (NaF, Sigma-Aldrich, ≥ 99%), serving for that latter as both fluorine and sodium source.

A series of $VOPO_4{\cdot}2H_2O$ powders were synthetized using a similar synthesis path where V_2O_5 was refluxed with H_3PO_4 in a round-bottom flask heated in an oil bath with a cooling column. Three different $VOPO_4{\cdot}2H_2O$ particles morphologies were obtained using three different synthesis media: acetone, deionized water and a mixture of deionized water and nitric acid. The resulting precursors were labelled $VOPO_4$ Acetone, $VOPO_4$ Water and $VOPO_4$ Nitric according to their synthesis medium. $VOPO_4$ Acetone was synthetized by refluxing 5 g of V_2O_5 with 6 ml of H_3PO_4 in 100 ml of acetone for 16h at 65°C. $VOPO_4$ Water was obtained by refluxing 2.4 g of V_2O_5 with 8 ml of H_3PO_4 in 100 ml of water at 104°C for 16h, followed by 6h of evaporation. Finally, the synthesis of $VOPO_4$ Nitric consisted of refluxing 3 g of V_2O_5 with 25 ml of H_3PO_4 in 150 ml of a 1:1 water:HNO_3 (in volume) (VWR Chemicals, wt. 65%) for 3h at 150°C. Each powder was washed (with acetone for $VOPO_4$ Acetone and water for the two others), recovered by centrifugation, and dried at 80 °C under air for one night.

Three $Na_3V_2(PO_4)_2FO_2$ ($NVPFO_2$) samples were synthetized by grounding in a mortar 665 mg of sodium fluoride with 1.9 g of one of the $VOPO_4{\cdot}2H_2O$ powders. A 10% excess of NaF was used compared to 1.5:1 stoichiometric molar ratio. Then, each mixture was introduced with 10 mL of 1-Ethyl-3-methylimidazolium tetrafluoroborate (EMIM-BF_4; IoLiTec, ≥ 99%) in a 45 mL Teflon Parr autoclave under air and heated at 220°C with a heating collar from IKA for 16 h under magnetic stirring. EMIM-BF_4 was selected as solvent for its good thermal stability up to 350°C and the BF_4^- anion's ability to act as a fluorine source through hydrolysis when it is in contact with the water molecules from the vanadium phosphate hydrate.[26,27] After the synthesis, the light green powder was washed with deionized water under stirring for 1h, retrieved by centrifugation and washed again for 1h in an ultrasonic bath of ethanol to get rid of any potential impurities. Each $NVPFO_2$ is referred by association with the corresponding $VOPO_4{\cdot}2H_2O$ precursor used for its synthesis (i.e. Acetone, Water or Nitric).

Additionally, an attempt was made to apply a carbon coating on the $NVPFO_2$ Acetone sample to further improve its electrochemical performance. To do so, the sample was pelletized and sintered under argon flow. The heating process consisted in two dwells, one at 250°C for 30 minutes and another at 600°C for 3 hours with a heating rate of 3°C/min. The resulting dark grey powder was sonicated for 1h in deionized water and dried at 80°C under air for one night and finally labeled as $NVPFO_2$A@C.

2.2 Characterization techniques

Powder X-ray Diffraction: A Panalytical Empyrean diffractometer in Bragg-Brentano θ-θ geometry, using a Cu $K\alpha_{1,2}$ type X-ray source was employed to measure the XRD patterns. The powders were analyzed using a spinning flat sample-holder in the 2θ range of 3°-100°(2θ) with a 0.0167° step size at room temperature. The Thompson-Cox-Hastings pseudo-Voigt function was chosen to perform the Le Bail and Rietveld refinements using the FullProf software.

Scanning Electron microscopy: To obtain information about the size and morphology of both the precursor and active material particles, a Tescan Vega scanning electron microscope was utilized. To avoid any charge effect, a thin gold layer was deposited at the surface of the samples prior to analysis.

Fourier-transform infrared spectroscopy: FTIR spectra were obtained on a Brucker Equinox 55 spectrometer in the 400-4000 cm^{-1} wavenumber range. For each sample, the analyzed powder had to be mixed with potassium bromide KBr in a 3:100 (wt.%) ratio respectively. A series of 30 acquisitions were performed for each sample to yield a better signal to noise ratio.

Raman spectroscopy: An Horiba confocal LabRAM HR Evolution micro-spectrometer, using a 633 nm laser source was employed to obtain Raman spectra. They were collected using a 10.6 mm (NA 0.5) focal length lens and with an acquisition time of 30 s and 30 accumulations. The spectrometer was calibrated prior measurement with a Si reference.

Tap Density measurements: An AUTOTAP from Quantachrome Instruments was utilized to measure the powders tap density in g/cm^3. Each sample was disposed in a 20 ± 0.1 mL graduated cylinder and tapped 10 000 times, with a quantity around 2 g. After the hits sequence, some particles that could stay not densified were removed in order to have a proper volume measurement. The tap density corresponds to the mass of $NVPFO_2$ in the graduated cylinder divided by the volume it occupies after the 10 000 hits.

BET analysis: Specific surface areas were determined by recording nitrogen sorption isotherms (77 K) with a 3Flex gas sorption analyzer (Micromeritics). Before analysis, the $NVPFO_2$ samples were degassed at 90 °C during 1 hour and at 150 °C during 14 hours, with ramp rates of 10 °C/min, under vacuum. Specific surface areas were obtained using the BET (Brunauer, Emmett and Teller) equation applied between 0.08 and 0.30 relative pressure (p/p0).

Transmission Electron Microscopy: The analyses were carried out on a TEM-JEOL 2200 FS FEG 200 kV in TEM mode. The analysed samples were disposed on a copper grid with a carbon supported film by deposing a droplet of the material suspension in ethanol.

X-ray Photoemission Spectroscopy: A ThermoFisher Scientific K-ALPHA spectrometer with a 400 μm X-Ray spot size and a monochromatized Al-Kα source (hν = 1486.6 eV) was used to acquire XPS spectra. The powders were pressed onto indium foils. The full spectra (0-1150 eV) were obtained with a constant pass energy of 200 eV, while high-resolution spectra were recorded with a constant pass energy of 40 eV. Charge neutralisation was applied during the analysis. High resolution spectra (i.e. C 1s, O 1s, V 2p, P 2p, Na 1s, F 1s, N 1s) were quantified using the Avantage software provided by ThermoFisher Scientific by applying Scofield sensitivity factors. All spectra were shifted versus C 1s main peak at 284.6 eV. Main attention was paid on N 1s, V $2p_{3/2}$ and F 1s spectra to get the chemical environment after fitting.

Electrochemistry: The $NVPFO_2$ electrochemical performance were evaluated using CR2032-type coin cells assembled in a glovebox under argon atmosphere. A slurry made from active material ($NVPFO_2$), carbon black and polyvinylidene fluorine (Sigma Aldrich) with a 80/10/10 ratio (wt.%) in N-methyl-2-pyrrolidone (Sigma Aldrich; 99% anhydrous) was prepared and casted with a doctor blade, set at a 200 μm thickness, on a carbon coated aluminum foil to obtain positive electrodes. These casted electrodes were dried overnight at 80°C under air. They were then cut in 16 mm diameter discs, pressed under 5 tons and dried under vacuum at 80°C for 2h before being stored in a glovebox under argon atmosphere. The $NVPFO_2$ electrodes were tested versus sodium metal, using as separator a Celgard foil between two Viledon ones soaked with the electrolyte 1 M $NaPF_6$ in 1:1 EC:DMC with 2% (wt.) content of fluoroethylene carbonate (FEC) as additive. The electrode mass loading was around 4.1 to 4.4 mg/cm². The coin cells were cycled in galvanostatic mode between 2.2 V and 4.3 V vs. Na^+/Na using a Biologic VMP cycler at a constant temperature of 25°C.

3. Results and discussion

3.1 Structural and morphological characterization

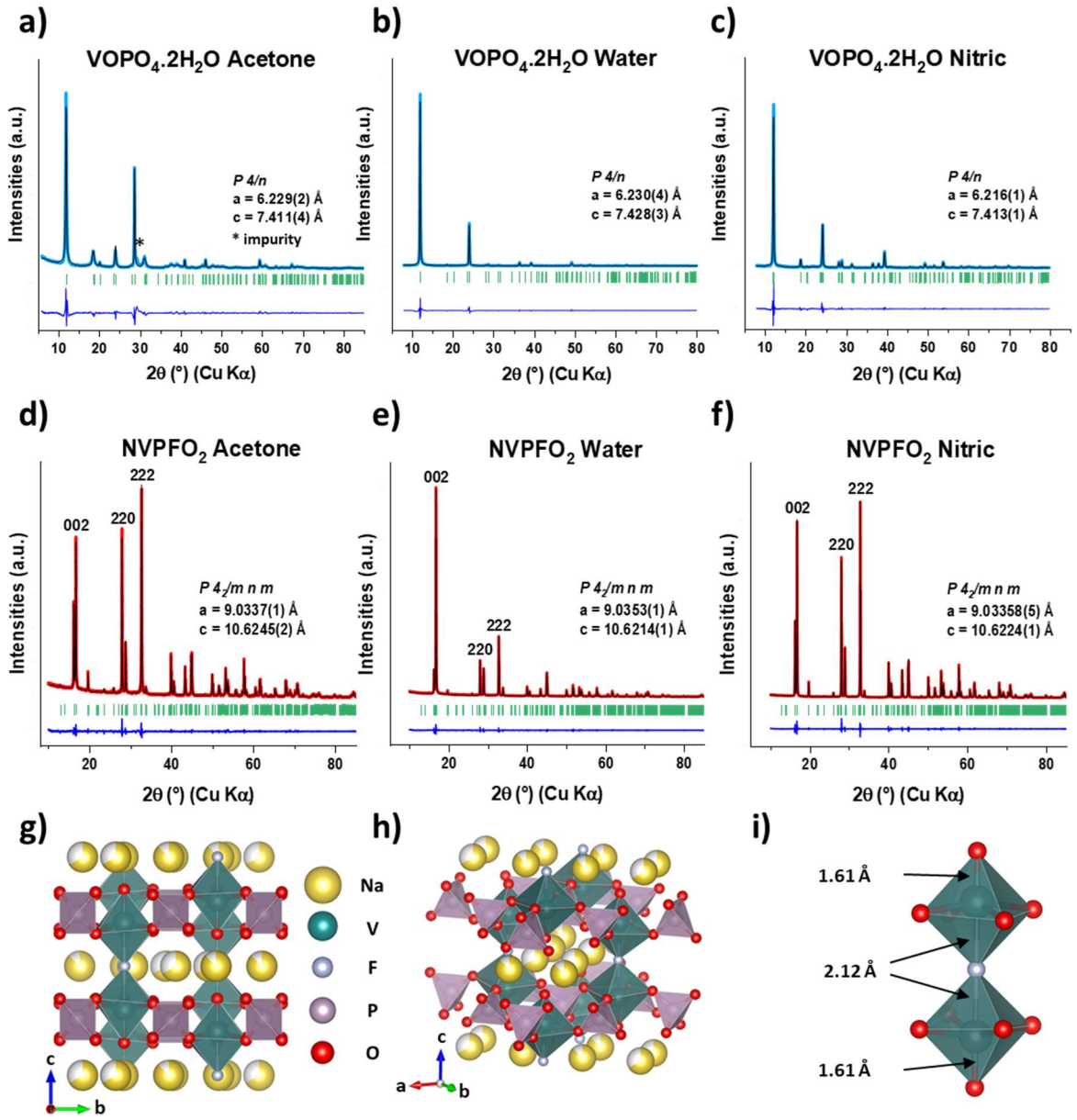

Figure 2: Full pattern matching refinements (Le Bail) obtained for a) $VOPO_4{\cdot}2H_2O$ Acetone, b) $VOPO_4{\cdot}2H_2O$ Water, c) $VOPO_4{\cdot}2H_2O$ Nitric, and the corresponding $NVPFO_2$ d) Acetone, e) Water, and f) Nitric. g-h) Representation of the crystal structure of $Na_3V_2(PO_4)_2FO_2$ with i) the V-F and V=O bond lengths in the bi-octahedron units.

Figure 2 displays the XRD patterns of the three different $NVPFO_2$ materials and their associated $VOPO_4{\cdot}2H_2O$ precursors. Focusing on the precursors, a preferential orientation can be observed on the XRD patterns of $VOPO_4{\cdot}2H_2O$ synthesized in water and nitric acid. These materials adopt a platelet shape that tends to grow along the <100> and <010> directions (Figure 3), resulting in an enhanced intensity of the 00*l* diffraction peak.[22,28] The $VOPO_4{\cdot}2H_2O$

Water exhibits platelets with diameters ranging from 1-2 µm for the smallest to almost 30 µm for the largest (Figure 3c) whereas for the $VOPO_4 \cdot 2H_2O$ Nitric the platelets have a rounded shape, with a diameter ranging from 1 to 15 µm and a thickness between 250 nm and 500 nm. In contrast, the $VOPO_4 \cdot 2H_2O$ Acetone particles exhibit a sheet-like morphology (Figure 3a) without any preferential orientation (Figure 2a). These aggregated sheets measure between 90 nm and 160 nm in thickness and 1 and 5 µm in diameter (Figure 3a).

Although the X-ray pattern of $VOPO_4 \cdot 2H_2O$ Acetone displayed a low intensity additional peak at ≈ 30° potentially coming from a $HVOPO_4$ impurity, for each $VOPO_4 \cdot 2H_2O$ precursor, the subsequent ionothermal synthesis of $Na_3V_2(PO_4)_2FO_2$ resulted in the formation of a pure phase. All diffraction peaks could be indexed in the *P*4_2*/mnm* space group (Figures 2d-f). The lattice parameters obtained from full pattern matching refinements (Table 1) are in good agreement with the V^{4+}-rich chemical composition $Na_3V_2(PO_4)_2FO_2$ as reported by Fang *et al.*[15]. For the $Na_3V_2(PO_4)_2F_{3-y}O_y$ family, the replacement of V-F bonds (1.968 Å)[29] by very short V=O vanadyl bonds (1.61 Å) (Figure 2i) results in a gradual reduction of the lattice size along the z axis. Therefore, as "*y*" or in other words, the fluorine content decreases, the *c* lattice parameter continuously decreases from 10.75 Å (y = 0) until reaching a value close to 10.62 Å for y = 2, as observed for our series of polyanionic materials (Figure S1).

Table 1: Lattice parameters, coherent domain sizes obtained by Le Bail refinement, tap density values and specific surface areas obtained for the three $NVPFO_2$ materials

Material	**a (Å)**	**c (Å)**	**V/Z (Å^3)**	**Coherent domain size (nm)**		**Tapped density (g/cm^3)**	**BET surface area (m²/g)**
				(002)	(220)		
$NVPFO_2$ Acetone	9.0337(1)	10.6245(2)	216.76	86	> 100	0.76	6.8(5)
$NVPFO_2$ Water	9.0353(1)	10.6214(1)	216.77	> 100	> 100	0.77	5.3(5)
$NVPFO_2$ Nitric	9.03358(5)	10.6238(8)	216.74	> 100	> 100	1.03	6.3(5)

The particles morphology of the $Na_3V_2(PO_4)_2FO_2$ differs from that of their corresponding $VOPO_4 \cdot 2H_2O$ precursors, but the nature of the latter still impacts the microstructure of the electrode material as evidenced by both XRD patterns and SEM images. For instance, the preferential orientation along the <002> direction is still very pronounced for $NVPFO_2$ Water material (Figure 2e) compared to the two others from the series.

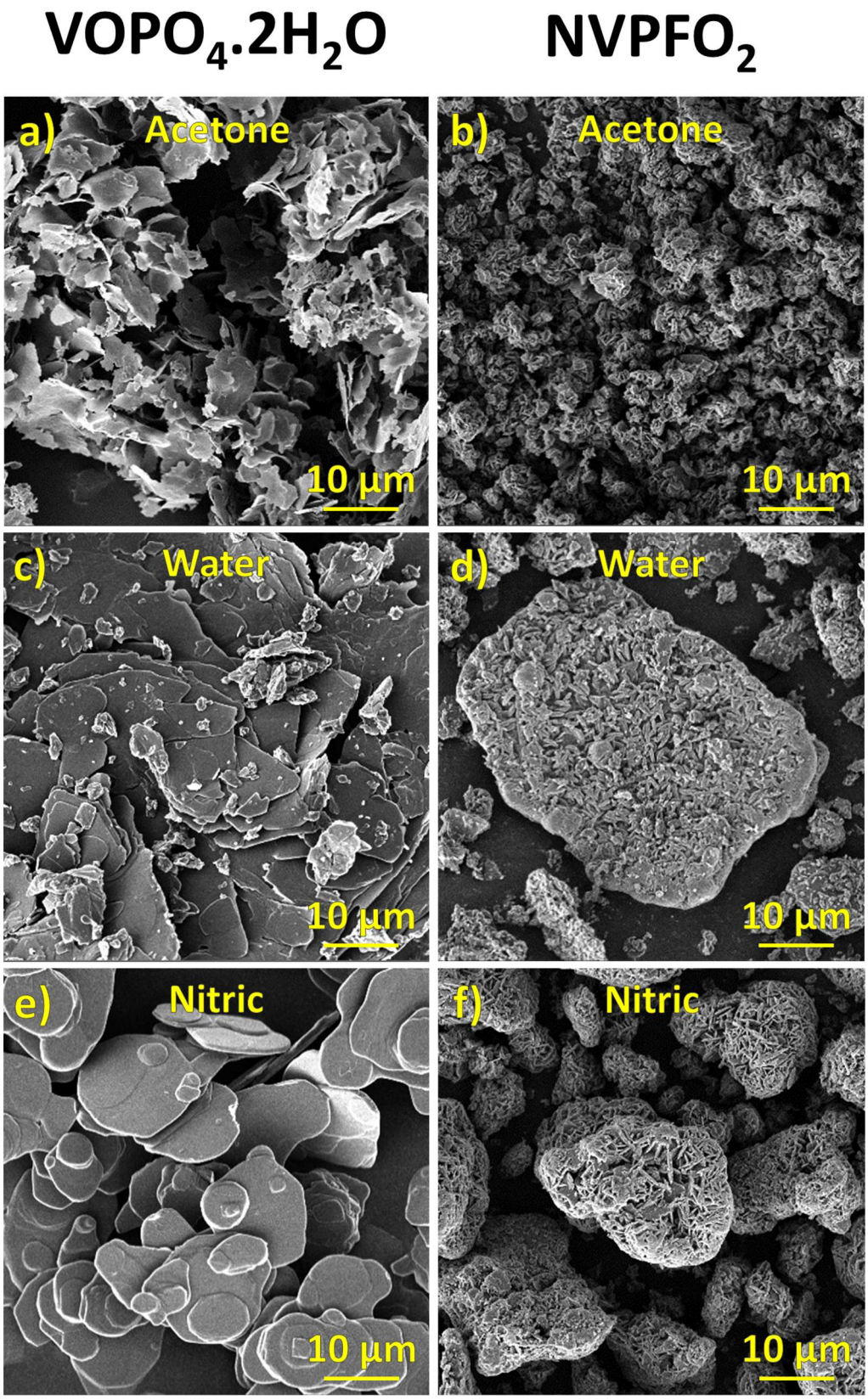

Figure 3: SEM images of the precursors $VOPO_4 \cdot 2H_2O$ a) Acetone, c) Water and e) Nitric along with the associated synthetized $NVPFO_2$ b) Acetone, d) Water and f) Nitric.

This observation is consistent with the morphology shown in Figure 3d, where large platelets (diameter of 7 to 35 µm and thickness of 2 µm) are covered by smaller agglomerated particles (300 nm to 500 nm thick), likely resulting from broken particles due to the continuous stirring during the synthesis. For $NVPFO_2$ Nitric, small platelets (300 nm to 550 nm thick) are agglomerated together to form secondary particles with a diameter ranging from 8 to 20 µm. Their rather spherical shape explains both the absence (loss) of preferential orientation (Figure 3f) and their higher tap density thanks to their morphology allowing a greater compaction (Table 1).

In contrast, the $NVPFO_2$ Acetone material consists of small platelets having a thickness between 120 nm and 300 nm that agglomerate in shapeless secondary particles with size ranging from 700 nm to 2.5 µm wide, as seen in the SEM images (Figure 3b). However, its tap density is comparable to that of the $NVPFO_2$ Water, due to the reduced compactness of the aggregates compared to the $NVPFO_2$ Nitric ones. $NVPFO_2$ Acetone also possesses the highest specific surface area of the series thanks to its peculiar particle morphology (Table 1). Additional SEM images are available in the supplementary information (Figures S2, S3 and S4).

Fourier Transform Infrared Spectroscopy analyses were also conducted on the series of $NVPFO_2$ (Figure 4a). First, characteristic vibrational bands for the $Na_3V_2(PO_4)_2FO_2$ phase clearly appear with an intense band at 1050 cm^{-1} associated to the phosphate groups and a doublet at 925 cm^{-1} and 945 cm^{-1} typical of the vanadyl V=O bonds vibrations.[12] Besides, the overtone at 1855 cm^{-1} is also attributed to the presence of vanadyl bonds. Furthermore, additional bands at 1440 cm^{-1} and in the 3000-3250 cm^{-1} region are observed across all spectra, corresponding to CH_3(N), N-H, C-H and O-H bonds vibrations, which are attributed to residual EMIM-BF_4 forming a thin layer on the surface of the $NVPFO_2$ materials.[22,30–32] Vibrations attributed to BF_4^- bonds coming from the ionic liquid-based layer can also be detected around 1084 cm^{-1} but these latter overlapped with bands attributed to phosphates.[33] The presence of this ionic liquid-based coating is confirmed by transmission electron microscopy imaging, as observed in Figure 4 b-e for $NVPFO_2$ Acetone. Although the thickness of the amorphous layer varies among the particles, the latter seems to cover their whole surfaces: none was found without an IL layer while scrutinizing the powder. Therefore, FTIR analyses along with TEM imaging confirm the presence of an ionic liquid-based coating on the particles surface, even after the washing step.

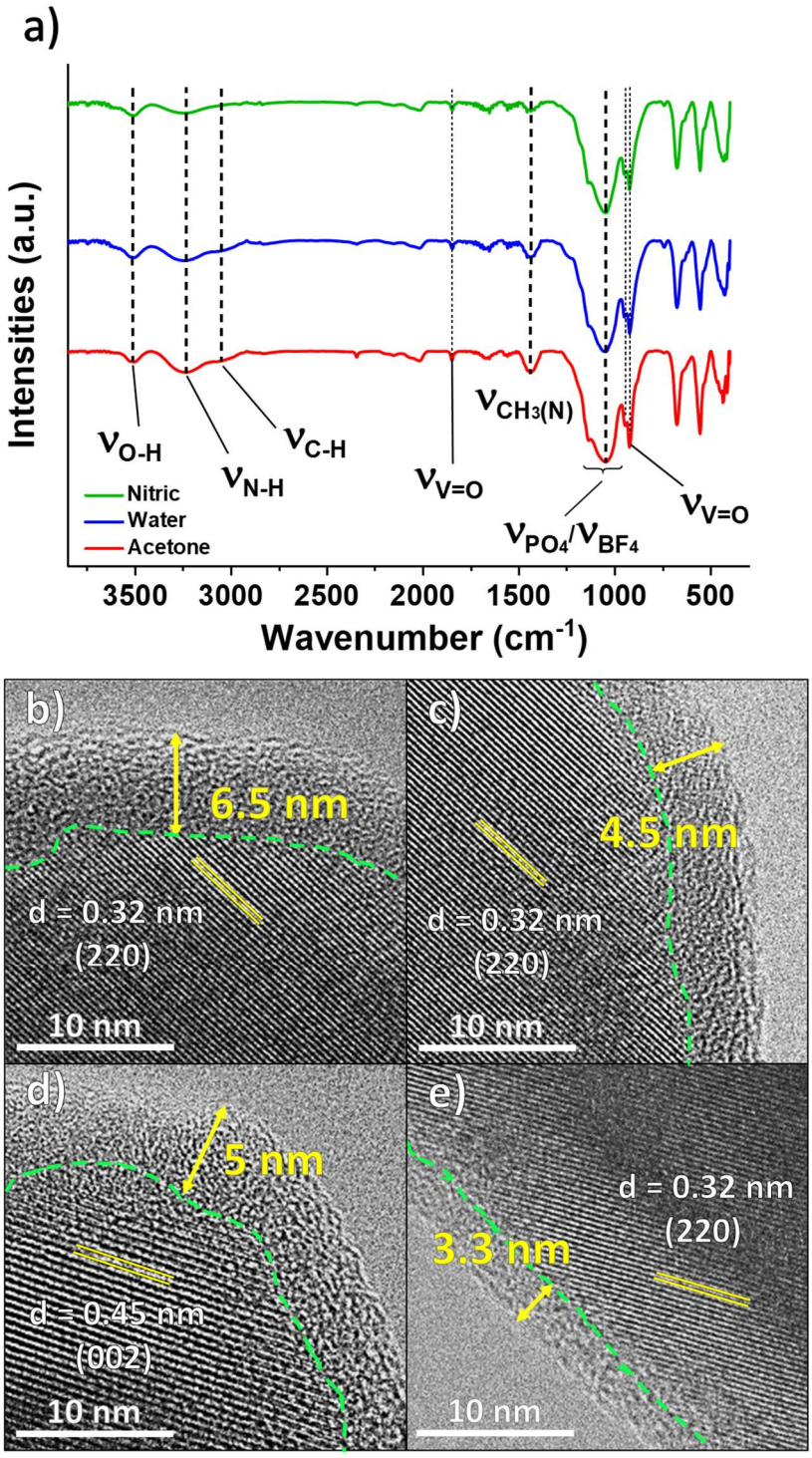

Figure 4: a) FTIR spectra recorded between 400 and 4000 cm^{-1} for the three $NVPFO_2$ materials Acetone (red), Water (blue) and Nitric (green). b) c) d) and e) Transmission electron microscopy images of the $NVPFO_2$ Acetone material. The atomic interplanar distance is given for each particle selected. The presence of an amorphous layer at their surface is also highlighted by a green dashed line, its thickness being given at different localizations.

Instinctively, one might think that the materials electrochemical performance could be hindered by this kind of coating. However, although its precise impact still has to be investigated, previous studies have shown that an organic layer from the ionic liquid can enhance ionic conductivity at the surface of the material and at grain boundaries,[13] thereby increasing delivered rate capabilities compared to IL coating free micrometric electrode material.

3.2 Electrochemical performance

Figure 5 displays the galvanostatic curves at different C-rates, the corresponding first cycle derivatives at C/20, the rate capability and capacity retention over 70 cycles for the three $NVPFO_2$ electrode materials. First, it can be noticed that all materials exhibit a similar electrochemical signature, characterized by two reversible (pseudo)plateaus at ≈ 3.6 and 4 V vs Na^+/Na (Figure 5a-f), in perfect agreement with previous reports.[6,22] Besides, at C/20 each material delivers a high specific capacity exceeding 115 mAh/g, which is close to the theoretical capacity of 130 mAh/g. Among them, $NVPFO_2$ Acetone material shows the best high rate performance (Figure 5g).

This enhanced performance can be attributed to the dispersed platelets morphology of the $NVPFO_2$ Acetone material, which optimizes the electrode/electrolyte interface and facilitates rapid sodium-ion insertion and extraction. [13,34,35] For example, at 1C, it achieves a specific capacity of 83 mAh/g, compared to 58 mAh/g and 56 mAh/g for $NVPFO_2$ Nitric and $NVPFO_2$ Water, respectively. In contrast, the very compact morphology of the $NVPFO_2$ Nitric material is disadvantageous for high rate cycling. Indeed, such organization of the primary platelets to form micro-sized agglomerates can hinder an efficient ionic diffusion within the aggregates, thus limiting the kinetic.

Finally, prolonged cycling tests revealed excellent capacity retention during long-term cycling at C/5, similar for all the materials, with a specific capacity loss of around 0.115 mAh/g per cycle. Therefore, considering these results and the better rate capability of $NVPFO_2$-Acetone, the latter appears to be the best performing electrode material.

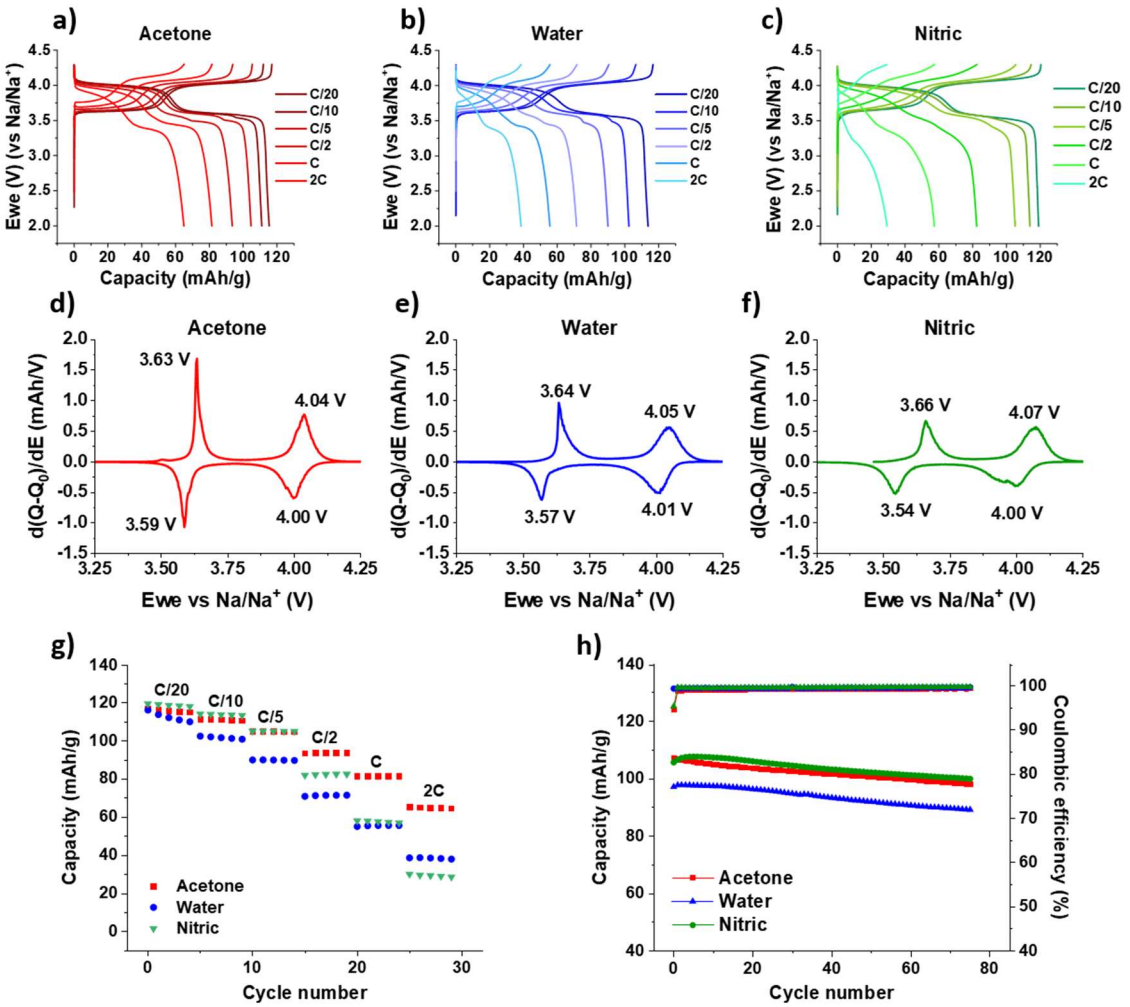

Figure 5: Galvanostatic curves at different cycling rates for $NVPFO_2$ a) Acetone, b) Water and c) Nitric; Corresponding dQ/dV derivatives versus potential of the first cycles performed at C/20 for $NVPFO_2$ d) Acetone, e) Water and f) Nitric; g) Capacity retention versus cycle number at different cycling rates and h) Capacity retention versus cycle number at C/5 for the three $NVPFO_2$ materials, Acetone (red), Water (blue) and Nitric (green).

3.3 Carbon coating formation by thermal degradation of the IL layer

Common strategies to improve the electrochemical performance of polyanionic active materials in batteries typically involve modifying both the morphology and the surface chemistry of the particles (e.g. nanosized carbon-coated $LiFePO_4$). The morphological aspect was explored in the first part of this paper, and the best candidate appeared to be the $NVPFO_2$ Acetone. Regarding its surface, FTIR and transmission electronic microscopy analyses demonstrated the presence of an ionic liquid layer on the $NVPFO_2$ particles (Figure 4), which can improve the ionic conductivity within the electrode[13]. However, polyanionic materials often suffer from a poor electronic conductivity, and one the most effective approaches to address

this issue is the formation of a conductive carbon coating.[36] The performance of these surface-modified materials strongly depends on the uniformity of the carbon layer, in coverage and in thickness, to ensure optimal electronic percolation between the particles in the electrode.[37] Most of the time, the carbon coating is obtained by mixing the active material with a solid carbon source such as glucose, followed by a thermal treatment at high temperature under argon flow or nitrogen. However, this method does not guarantee the formation of a uniform layer.[38] In contrast, using gels or liquid carbon sources enables it, thereby enhancing electrochemical performance.[38,39] Therefore, carbonizing the ionic liquid layer that perfectly covers the particles of $NVPFO_2$ Acetone material should greatly improve its performance, considering that it was already demonstrated that ionic liquids are efficient precursors for carbon coatings.[40,41]

During the thermal sintering, the absorbed water and other chemical species containing oxygen and hydrogen are expected to be extracted during the first thermal dwell at 250°C, in order to limit the carbon coating oxidation. Thereafter on the second dwell, the remaining organic matter will be decomposed and carbonize to form the graphitized carbon coating on the particles. After the thermal treatment of $NVPFO_2$ Acetone (leading to $NVPFO_2$A@C), an increase of the *c* lattice parameter can be noticed (Figure 6a), indicating a decrease of the oxygen content to y = 1.7 (Figure S1). This change was attributed to a fluorination induced by the BF_4^- anion decomposition from the ionic liquid, leading to a partial vanadium reduction for charge compensation. Indeed, it is believed that BF_4^- is decomposed into one F^- anion that will be incorporated into the bulk of the materials and BF_3 gas which will be evacuated with the argon flow. This result demonstrates the potential of fluorinated ionic liquids to generate fluorine *in situ* during the synthesis and to fluorinate material post synthesis with a simple annealing step.

Regarding the morphology, the small platelet agglomerates were preserved (Figure 6b). Further analyses indicate the successful carbonization of the ionic liquid-based layer. FTIR analyses revealed the disappearance of the vibrational bands related to the O-H and C-H bonds (Figure 6c), while Raman spectroscopy analyses showed the emergence of two broad signals attributed to the D and G bands of carbon, which are characteristic of a disordered graphitized carbon layer (Figure 6d).[38] However, a Raman mapping (with a lateral resolution of ≈ 1 µm) revealed relative intensity variations in these D and G bands (compared to bands attributed to phosphates) depending on the location on the sample, indicating a coating thickness inhomogeneity. Indeed, the high relative intensity of the V=O and P-O vibrational bands (versus D- and G-bands) show locally a low amount of carbon at the surface of the particles (Figure

S5). Moreover, the ratio $I_D/I_G \approx 2$ calculated through the D- and G-band fitting, indicates a high degree of disordering, in line with the rather low annealing temperature of 600°C.[42]

Finally, thermogravimetric analysis (TGA) under air of the $NVPFO_2A@C$ showed that the weight fraction of the carbon coating was around 0.25% (Figure S6), which might explain that transmission electronic microscopy imaging did not provide conclusive results for direct observation of the carbon layer (Figure S7). These results suggest that a thin and potentially inhomogeneous in thickness carbon coating was formed during the thermal treatment.

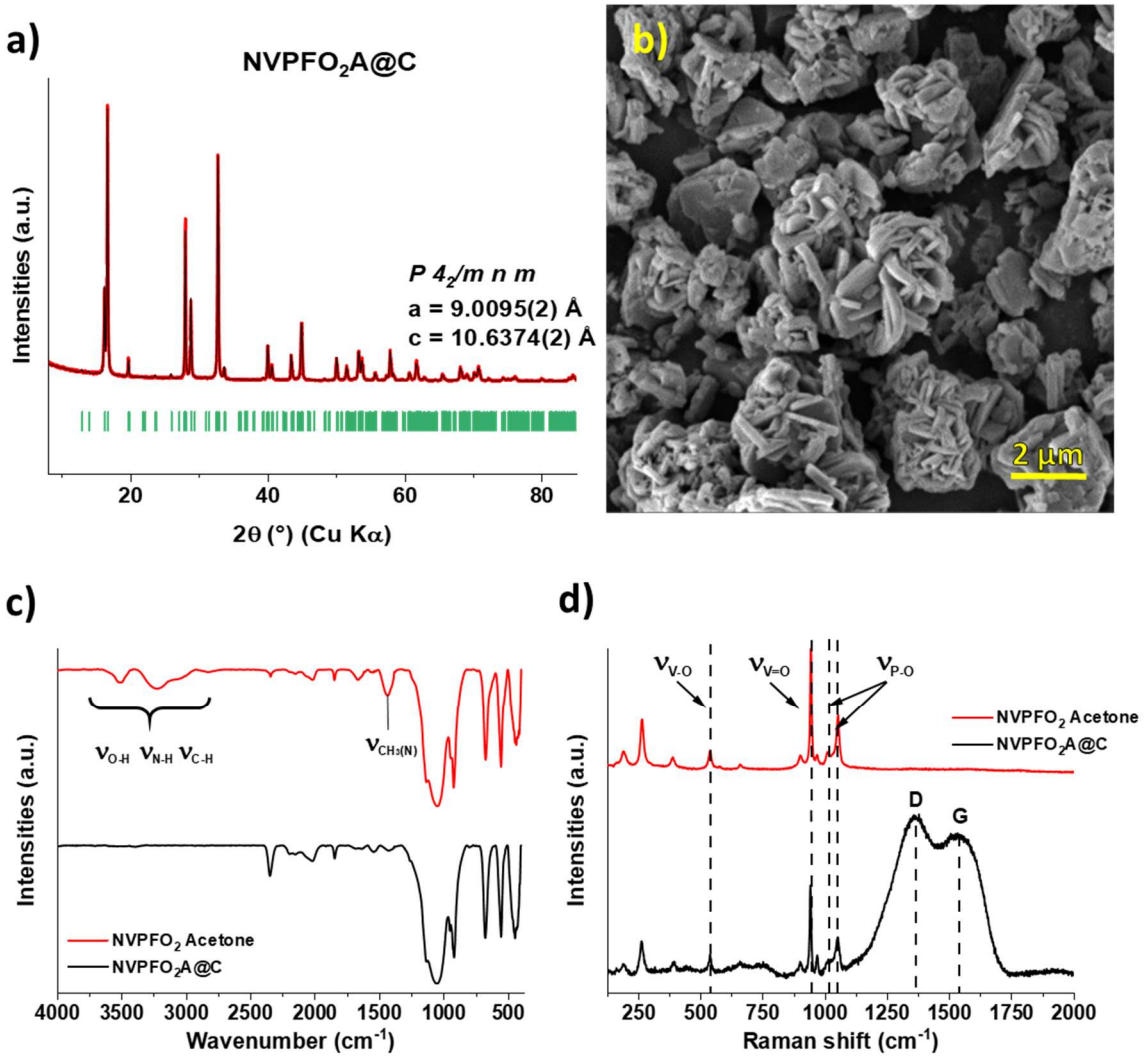

Figure 6: a) Full X-ray diffraction pattern matching (Le Bail) and b) SEM image for the $NVPFO_2@C$ material, c) FTIR and d) Raman spectra of the material before (red) and after (black) sintering.

A comparative X-ray photoemission spectroscopy study was also conducted to examine the surface chemistry of the material before and after the thermal treatment under argon. The N 1s, F 1s and V $2p_{3/2}$ XPS spectra are displayed in Figure 7, the surface atomic quantifications of both materials are reported in Table S1. First, it can be noticed that for the pristine material (before annealing), the N/C atomic ratio is different from the ionic liquid composition (1/10 versus 1/3 respectively), which shows that other organic species than EMIM BF_4 are also present at the material surface. The presence of the ionic liquid is confirmed by the peak at 401.7 eV on the N1s spectra related to the nitrogen in the EMIM imidazole ring (Figure 7b).[33,43] The second peak at 399.8 eV is certainly related to amine or even reduced nitrogen species, such as in the case of a deprotonated C4 carbon as proposed in the literature.[44,45] After the heat treatment, the nitrogen amount is highly reduced but still present, the remaining small peaks at 399.8 eV and 402 eV were associated to pyrrolic and graphitic nitrogen respectively, indicating the N-doped character of the obtained carbon coating with a 2% (at.) doping.[46,47]

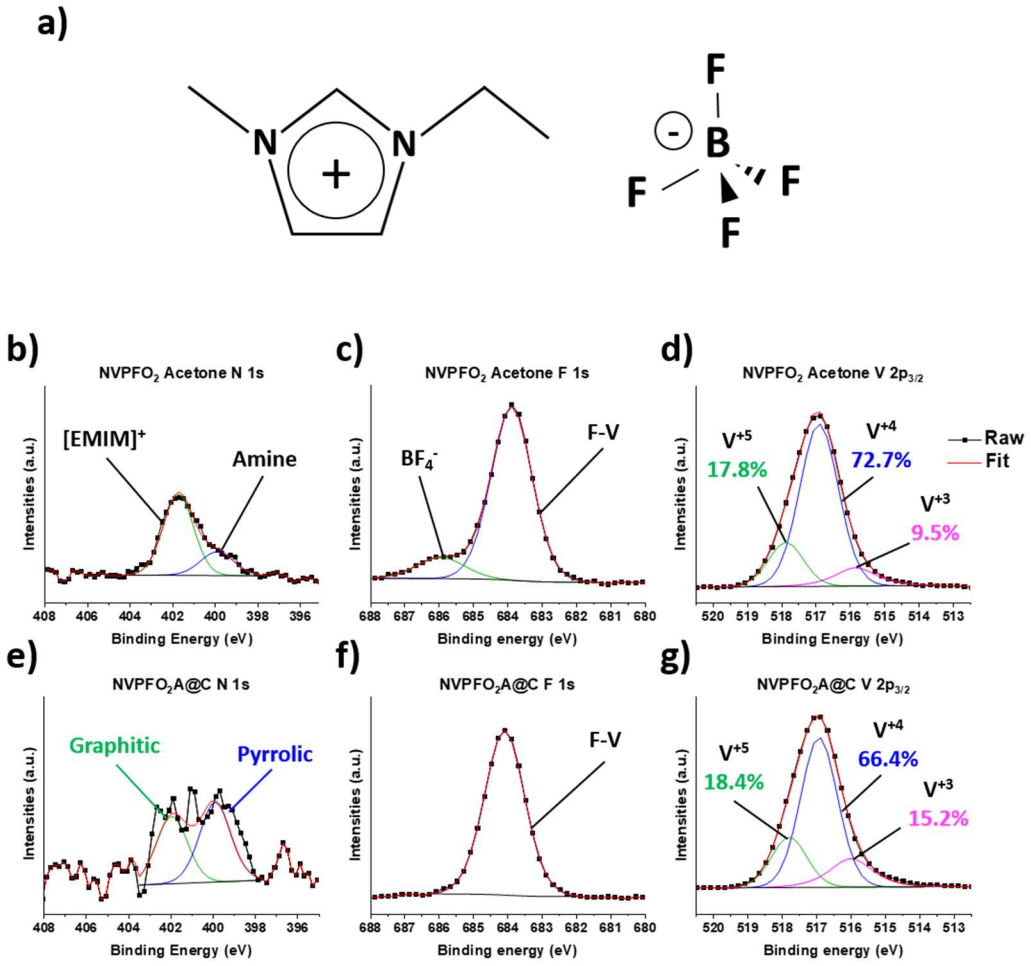

Figure 7: a) Schematic representation of the EMIM BF_4 ionic liquid; XPS N 1s, F 1s and V $2p_{3/2}$ spectra of b), c), d) $NVPFO_2$ Acetone and of e), f), g) $NVPFO_2$A@C respectively.

The $NVPFO_2$ Acetone F 1s spectra also confirms the ionic liquid presence, with a typical peak around 686 eV associated to the BF_4^- anion,[33] which disappeared after the sintering step, leading to the material fluorination and explaining why on the V $2p_{3/2}$ spectra, the vanadium mean oxidation state decreases for the $NVPFO_2A@C$ (Figure S8). Besides, this reduction is supported by the lattice parameters variation.

Finally, the C1s spectra exhibit different profiles (Figure S9), with an increase of peak at 284.5 eV after the heat treatment, related to the C=C sp^2 bonds in the conductive graphitized carbon for the $NVPFO_2A@C$.[48] Moreover, it can be noticed that the intensities of the peaks related to the C-C sp^3, C-O, C=O and O-C=O bonds are relatively important. Despite the fact that the C-O/N and C=O/N bonds content is decreased from 32 at.% to 17.3 at.% in the coating during the sintering (Table S2), the O-C=O bonds content is increased from 7.3 to 11.2 at.%, showing a highly oxidized and disordered state of the carbon in good agreement with Raman analysis.

Comparative electrochemical curves of $NVPFO_2$ Acetone versus $NVPFO_2A@C$ are displayed in Figure 8, the sintered material exhibits the highest specific capacity, very close to the theoretical value (Figure 8a). Furthermore, the dQ/dV derivative curves reveal a slight change into the sodium insertion and extraction mechanisms due to the change in O/F composition of the material (Figure 8b).[49] The first derivative signature of $NVPFO_2A@C$ is characterized by two broad peaks supporting solid solution type reactions whereas the sharp peak for the low voltage plateau for $NVPFO_2$ Acetone suggests the presence of biphased reactions.[6] This is in good agreement with previous observations made for the series of compounds $Na_3V_2(PO_4)_2F_{3-y}O_y$ ($0 \leq y \leq 2$): biphasic reactions are only associated to charge and alkali orderings for $y = 0$ (V^{3+} only) or $y = 2$ (V^{4+} only), whereas solid solution reactions are observed for the mixed valence V^{3+}/V^{4+} intermediate compositions ($0 < y < 2$).[6,9] Regarding the long-term cycling at C/5, both $NVPFO_2$ Acetone and $NVPFO_2A@C$ exhibit a similar excellent capacity retention, with however a much higher initial specific capacity of 123 mAh/g for the $NVPFO_2A@C$ versus 107 mAh/g for the $NVPFO_2$ Acetone (Figure 8c).

Rate capability tests were also conducted (Figure 8d), and they demonstrate that the thermal sintering can be beneficial for the electrochemical performance when comparing $NVPFO_2$ Acetone with $NVPFO_2A@C$, with specific capacity still around 88 mAh/g at 2C versus 62 mAh/g for $NVPFO_2$ Acetone. Note that higher galvanostatic charge/discharge rates were also tested but the use of Na metal as reference and negative electrode could not allow to obtain reproducible results (see Figure S10). The impedance spectroscopy results (Figure 8e) revealed that a smaller high-frequency semi-circle is observed for the $NVPFO_2A@C$ indicating a lower

charge transfer resistance and thus a better electronic conductivity, which aligns with rate capability results with a higher exhibited capacity at different cycling rates. In conclusion, a carbon layer on the polyanionic particle surface is more efficient compared to an IL based one for optimizing energy storage performance of electrode polyanionic materials. Besides, carbonizing the ionic liquid layer on the surface of the active material is a promising strategy to enhance electrochemical performance using only the solvent as a carbon source. In the future, it could be interesting to see if using an ionic liquid with longer alkyl chains or with different anions would increase the coating homogeneity or add other dopant which may result in even better performance.

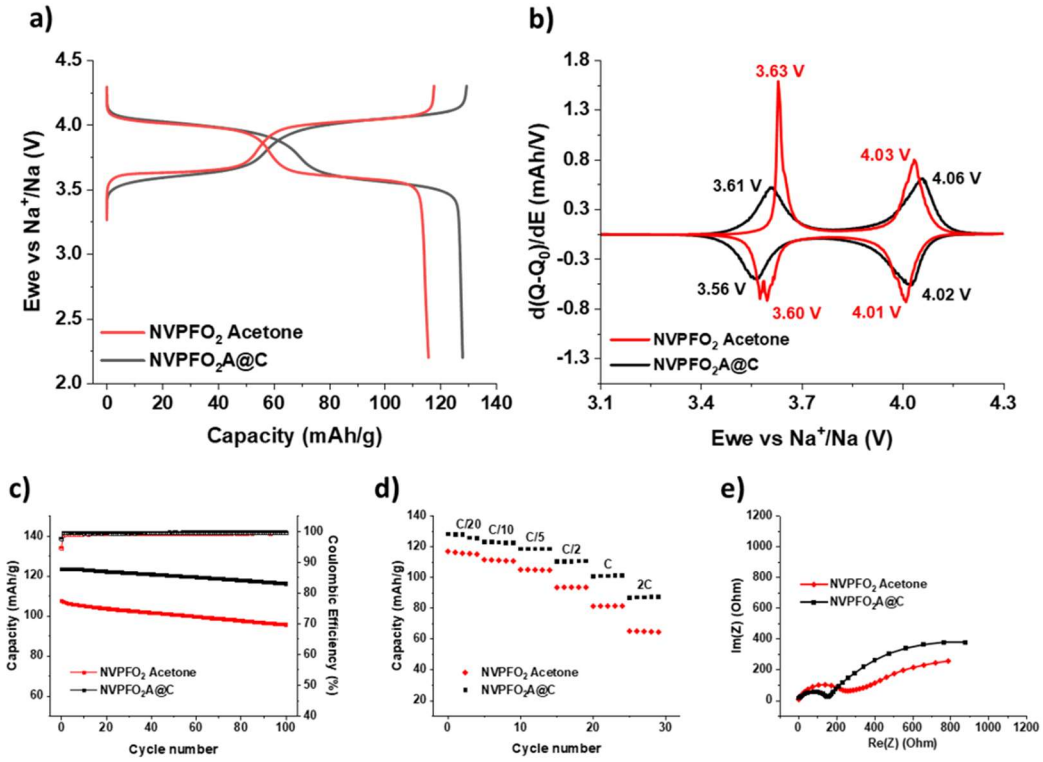

Figure 8: a) Galvanostatic curves of the 3rd cycle obtained at C/20 for $NVPFO_2$ Acetone and $NVPFO_2$A@C, b) Potential derivative curves of the 3rd cycle at C/20 for $NVPFO_2$ Acetone and $NVPFO_2$A@C, c) Capacity retention and coulombic efficiency at a rate of C/5 for 100 cycles, d) Capacity retention at different C-rates and e) Nyquist plots obtained for both $NVPFO_2$ Acetone and $NVPFO_2$A@C using EIS conducted after 3 galvanostatic cycles at C/20.

Finally, regarding the topochemical reaction in ionic liquid for the synthesis of $NVPFO_2$ as reported in this work, several arguments can be brought to illustrate the advantages of such process. First, ionic liquids offer increased safety due to their negligible vapor pressure and thermal stability up to moderate-to-high temperatures (250–350°C). This contrasts with

conventional solvothermal synthesis employing solvents such as water and ethanol, which pose higher risk due to the high-pressure conditions generated in the autoclave. Moreover, compared to water or ethanol, which have heat capacities of 4188 $J.kg^{-1}.K^{-1}$ at 290 K[50] and 2381 $J.kg^{-1}.K^{-1}$ at 300 K[51] respectively, ionic liquids generally require less energy for heating.[52] For instance, Sanmamed *et al.*[53] reported that the heat capacity of EMIM BF_4 ranges from 300 $J.mol^{-1}.K^{-1}$ (1515 $J.kg^{-1}.K^{-1}$) to 314 $J.mol^{-1}.K^{-1}$ (1586 $J.kg^{-1}.K^{-1}$) between 283.15 K and 323.15 K.

Additionally, this process is simpler than the well-established solid-state synthesis process, which involves multiple steps. For example, the synthesis of $VOPO_4 \cdot 2H_2O$ precursors, followed by dehydration or reduction to obtain $VOPO_4$ or VPO_4, adds additional steps before mixing with NaF to produce $Na_3V_2(PO_4)_2F_{3-y}O_y$ ($0 \leq y \leq 2$) materials.[8,9,49] Then, the rather low synthesis temperature of 220°C is very interesting in terms of energy consumption, while solid state route requires high temperatures between 600°C and 650°C and even at higher temperatures to obtain the VPO_4 precursor.[8,9]

The resulting plate-like morphology, oriented along the (a,b) planes, also enhances sodium diffusion. Indeed, due the platelets agglomeration, a different direction of diffusion such as along the platelets thickness (orientation along the (a,c) or (b,c) planes) could actually impede the Na^+ to properly be extracted from the active material particles despite the reduction of the diffusion length within the material bulk as demonstrated by Fang *et al*[15].

Finally, by adding these advantages with the possibility to transform the ionic liquid layer into a carbon coating, the synthesis of $Na_3V_2(PO_4)_2F_{3-y}O_y$ ($0 \leq y \leq 2$) phases in ionic liquids medium appears to be a promising method to obtain pure and efficient active material for Na-ion batteries.

4. Conclusion

A series of $VOPO_4 \cdot 2H_2O$ powders with distinct particles morphologies were synthetized and used as precursors to obtain three $Na_3V_2(PO_4)_2FO_2$ materials via topochemical reaction, each with specific particles size and shape. Due to these specific synthesis conditions and the peculiar 2D morphology of the precursor, the three active materials possess platelets shape particles with varying size and organization as characterized by SEM. FTIR and TEM analyses revealed that the three powders are encapsulated in an ionic liquid-based layer, which actually can be beneficial for the energy storage applications. Electrochemical tests in galvanostatic conditions showed that all three materials deliver high capacities at low cycling rate, however, the $NVPFO_2$ synthetized from the $VOPO_4 \cdot 2H_2O$ Acetone precursor exhibits the best capacity retention due to its more favourable particle size and particles agglomeration. The latter was selected to explore the feasibility of applying a carbon coating by carbonizing the ionic liquid coating without any additional carbon source. The resulting product exhibits slightly different lattice parameters than the pristine one, revealing a change in the fluorine/oxygen composition during the thermal treatment, as also confirmed by changes in the electrochemical signatures. Regarding the carbonization of the ionic liquid layer, preliminary results demonstrate the potential of this process with a consequent increase of the specific capacity and rate capability. However, an optimization is still needed to enhance the coating homogeneity.

In conclusion, the topochemical synthesis of $Na_3V_2(PO_4)_2FO_2$ in ionothermal conditions offers a promising approach for controlling particle morphology by manipulating the reaction conditions used to synthetize the precursor. Concerning the surface modification by the formation of a carbon coating, the use of an ionic liquid-based layer as a carbon source appears to be very promising, especially due to the extremely large number of different ionic liquids that can be obtained that is estimated up to 10^{12} possible cations and anions combinations.[23]

Supporting Information

The Supporting Information is available free of charge at
It contains the experimental section, the composition versus lattice parameters (c and *V/Z*) curves, the SEM images, the Raman spectra, the TGA analysis and the XPS, the $NVPFO_2$A@C TEM images, the XPS surface atomic quantification, the C 1s and V $2p_{3/2}$ spectra comparison.

ACKNOWLEDGMENTS

The authors would like to thank the French National Research Agency (STORE-EX Labex Project ANR-10-LABX-76-01 and Project Nano-INSPIRE ANR-21-CE50-0006) and the Materials Characterization Platform of the Région Nouvelle Aquitaine (PLACAMAT). The authors would also like to thank Étienne Durand, Emmanuel Petit, Jérôme Kalisky, Alexandre Fargues, and Eric Lebraud for their help with TGA, SEM, electrochemical characterizations, FTIR, and XRD.

References:

(1) Hu, Y.; Komaba, S.; Forsyth, M.; Johnson, C.; Rojo, T. A New Emerging Technology: Na-Ion Batteries. *Small Methods* **2019**, *3* (4), 1900184–1900184. https://doi.org/10.1002/smtd.201900184.

(2) Rudola, A.; Rennie, A. J. R.; Heap, R.; Meysami, S. S.; Lowbridge, A.; Mazzali, F.; Sayers, R.; Wright, C. J.; Barker, J. Commercialisation of High Energy Density Sodium-Ion Batteries: Faradion's Journey and Outlook. *J. Mater. Chem. A* **2021**, *9* (13), 8279–8302. https://doi.org/10.1039/D1TA00376C.

(3) Tarascon, J.-M. Na-Ion versus Li-Ion Batteries: Complementarity Rather than Competitiveness. *Joule* **2020**, *4* (8), 1616–1620. https://doi.org/10.1016/j.joule.2020.06.003.

(4) Hasa, I.; Mariyappan, S.; Saurel, D.; Adelhelm, P.; Koposov, A. Y.; Masquelier, C.; Croguennec, L.; Casas-Cabanas, M. Challenges of Today for Na-Based Batteries of the Future: From Materials to Cell Metrics. *Journal of Power Sources* **2021**, *482*, 228872. https://doi.org/10.1016/j.jpowsour.2020.228872.

(5) Broux, T.; Fauth, F.; Hall, N.; Chatillon, Y.; Bianchini, M.; Bamine, T.; Leriche, J.; Suard, E.; Carlier, D.; Reynier, Y.; Simonin, L.; Masquelier, C.; Croguennec, L. High Rate Performance for Carbon-Coated $Na_3V_2(PO_4)_2F_3$ in Na-Ion Batteries. *Small Methods* **2019**, *3* (4), 1800215. https://doi.org/10.1002/smtd.201800215.

(6) Nguyen, L. H. B.; Broux, T.; Camacho, P. S.; Denux, D.; Bourgeois, L.; Belin, S.; Iadecola, A.; Fauth, F.; Carlier, D.; Olchowka, J.; Masquelier, C.; Croguennec, L. Stability in Water and Electrochemical Properties of the $Na_3V_2(PO_4)_2F_3$ – $Na_3(VO)_2(PO_4)_2F$ Solid Solution. *Energy Storage Materials* **2019**, *20*, 324–334. https://doi.org/10.1016/j.ensm.2019.04.010.

(7) Serras, P.; Palomares, V.; Alonso, J.; Sharma, N.; López Del Amo, J. M.; Kubiak, P.; Fdez-Gubieda, M. L.; Rojo, T. Electrochemical Na Extraction/Insertion of $Na_3V_2O_{2x}(PO_4)_2F_{3-2x}$. *Chem. Mater.* **2013**, *25* (24), 4917–4925. https://doi.org/10.1021/cm403679b.

(8) Pablos, C.; Olchowka, J.; Petit, E.; Minart, G.; Duttine, M.; Weill, F.; Masquelier, C.; Carlier, D.; Croguennec, L. Thermal Stability of $Na_{3-x}V_2(PO_4)_2F_{3-y}O_y$: Influence of F^- for O^{2-} Substitution and Degradation Mechanisms. *Chem. Mater.* **2023**, *35* (10), 4078–4088. https://doi.org/10.1021/acs.chemmater.3c00539.

(9) Akhtar, M.; Arraghraghi, H.; Kunz, S.; Wang, Q.; Bianchini, M. A Novel Solid-State Synthesis Route for High Voltage $Na_3V_2(PO_4)_2F_{3-2y}O_{2y}$ Cathode Materials for Na-Ion Batteries. *J. Mater. Chem. A* **2023**, *11* (46), 25650–25661. https://doi.org/10.1039/D3TA04239A.

(10) Kumar, P. R.; Jung, Y. H.; Lim, C. H.; Kim, D. K. $Na_3V_2O_{2x}(PO_4)_2F_{3-2x}$: A Stable and High-Voltage Cathode Material for Aqueous Sodium-Ion Batteries with High Energy Density. *J. Mater. Chem. A* **2015**, *3* (12), 6271–6275. https://doi.org/10.1039/C5TA00980D.

(11) Broux, T.; Fleutot, B.; David, R.; Brüll, A.; Veber, P.; Fauth, F.; Courty, M.; Croguennec, L.; Masquelier, C. Temperature Dependence of Structural and Transport Properties for $Na_3V_2(PO_4)_2F_3$ and $Na_3V_2(PO_4)_2F_{2.5}O_{0.5}$ *Chem. Mater.* **2018**, *30* (2), 358–365. https://doi.org/10.1021/acs.chemmater.7b03529.

(12) Fang, R.; Olchowka, J.; Pablos, C.; Bianchini Nuernberg, R.; Croguennec, L.; Cassaignon, S. Impact of the F^- for O^{2-} Substitution in $Na_3V_2(PO_4)_2F_{3-y}O_y$ on Their Transport Properties and Electrochemical Performance. *ACS Appl. Energy Mater.* **2022**, *5* (1), 1065–1075. https://doi.org/10.1021/acsaem.1c03446.

(13) Olchowka, J.; Fang, R.; Bianchini Nuernberg, R.; Pablos, C.; Carlier, D.; Cassaignon, S.; Croguennec, L. Particle Nanosizing and Coating with an Ionic Liquid: Two Routes to Improve the Transport Properties of $Na_3V_2(PO_4)_2FO_2$. *Nanoscale* **2022**, *14* (24), 8663–8676. https://doi.org/10.1039/D2NR01080A.

(14) Mukherjee, A.; Sharabani, T.; Sharma, R.; Okashy, S.; Noked, M. Effect of Crystal Structure and Morphology on $Na_3V_2(PO_4)_2F_3$ Performances for Na-Ion Batteries. *Batteries and Supercaps* **2020**, *3* (6), 510–518. https://doi.org/10.1002/batt.201900202.

(15) Fang, R.; Olchowka, J.; Pablos, C.; Camacho, P. S.; Carlier, D.; Croguennec, L.; Cassaignon, S. Effect of the Particles Morphology on the Electrochemical Performance of $Na_3V_2(PO_4)_2F_{3-y}O_y$. *Batteries & Supercaps* **2022**, *5* (1). https://doi.org/10.1002/batt.202100179.

(16) Wang, M.; Wang, Y.; Xin, Y.; Liu, Q.; Wu, F.; Gao, H. Nitrogen-Doped Carbon Coated $Na_3V_2(PO_4)_2F_3$ Derived from Polyvinylpyrrolidone as a High-Performance Cathode for Sodium-Ion Batteries. *ACS Appl. Energy Mater.* **2023**, *6* (8), 4453–4461. https://doi.org/10.1021/acsaem.3c00605.
(17) Lu, T.; Yu, X.; Li, X.; Qi, J.; Huang, S.; Man, Z.; Zhuo, H. Zwitterionic Polymer-Derived Nitrogen and Sulfur Co-Doped Carbon-Coated $Na_3V_2(PO_4)_2F_3$ as a Cathode Material for Sodium Ion Battery Energy Storage. *New Journal of Chemistry* **2021**, *45* (41), 19391–19401. https://doi.org/10.1039/D1NJ03779J.
(18) Liu, W.; Yi, H.; Zheng, Q.; Li, X.; Zhang, H. Y-Doped $Na_3V_2(PO_4)_2F_3$ Compounds for Sodium Ion Battery Cathodes: Electrochemical Performance and Analysis of Kinetic Properties. *J. Mater. Chem. A* **2017**, *5* (22), 10928–10935. https://doi.org/10.1039/C7TA03133E.
(19) Essehli, R.; Yahia, H. B.; Amin, R.; Li, M.; Morales, D.; Greenbaum, S. G.; Abouimrane, A.; Parejiya, A.; Mahmoud, A.; Boulahya, K.; Dixit, M.; Belharouak, I. Sodium Rich Vanadium Oxy-Fluorophosphate – $Na_{3.2}Ni_{0.2}V_{1.8}(PO_4)_2F_2O$ – as Advanced Cathode for Sodium Ion Batteries. *Advanced Science* **2023**, *10* (22), 2301091. https://doi.org/10.1002/advs.202301091.
(20) Nguyen, L. H. B.; Olchowka, J.; Belin, S.; Sanz Camacho, P.; Duttine, M.; Iadecola, A.; Fauth, F.; Carlier, D.; Masquelier, C.; Croguennec, L. Monitoring the Crystal Structure and the Electrochemical Properties of $Na_3(VO)_2(PO_4)_2F$ through Fe^{3+} Substitution. *ACS Appl. Mater. Interfaces* **2019**, *11* (42), 38808–38818. https://doi.org/10.1021/acsami.9b14249.
(21) Minart, G.; Croguennec, L.; Weill, F.; Labrugère-Sarroste, C.; Olchowka, J. Increasing Tap Density of Carbon-Coated $Na_3V_2(PO_4)_2F_3$ via Mechanical Grinding: Good or Bad Idea? *ACS Appl. Energy Mater.* **2024**, *7* (24), 11334-11342. https://doi.org/10.1021/acsaem.3c03230.
(22) Olchowka, J.; Nguyen, L. H. B.; Petit, E.; Camacho, P. S.; Masquelier, C.; Carlier, D.; Croguennec, L. Ionothermal Synthesis of Polyanionic Electrode Material $Na_3V_2(PO_4)_2FO_2$ through a Topotactic Reaction. *Inorg. Chem.* **2020**, *59* (23), 17282–17290. https://doi.org/10.1021/acs.inorgchem.0c02546.
(23) Forsyth, Stewart A., Jennifer M. Pringle, and Douglas R. MacFarlane. "Ionic Liquids—an Overview." Australian Journal of Chemistry **2004**, 57 (2), 113-119. https://doi.Org/10.1071/CH03231.
(24) Eshetu, G. G.; Armand, Michel.; Ohno, Hiroyuki.; Scrosati, Bruno.; Passerini, S. Ionic Liquids as Tailored Media for the Synthesis and Processing of Energy Conversion Materials. *Energy Environ. Sci.* **2016**, *9* (1), 49–61. https://doi.org/10.1039/C5EE02284C.
(25) Recham, N.; Dupont, L.; Courty, M.; Djellab, K.; Larcher, D.; Armand, M.; Tarascon, J.-M. Ionothermal Synthesis of Tailor-Made $LiFePO_4$ Powders for Li-Ion Battery Applications. *Chem. Mater.* **2009**, *21* (6), 1096–1107. https://doi.org/10.1021/cm803259x.
(26) Olchowka, J.; Hagemann, H.; Delgado, T.; Wickleder, C. The Influence of Ionothermal Synthesis Using $BmimBF_4$ as a Solvent on Nanophosphor $BaFBr:Eu^{2+}$ Photoluminescence. *Nanoscale* **2018**, *10* (42), 19706–19710. https://doi.org/10.1039/C8NR06842A.
(27) Olchowka, J.; Suta, M.; Wickleder, C. Green Synthesis of A_2SiF_6 (A=Li–Cs) Nanoparticles Using Ionic Liquids as Solvents and as Fluorine Sources: A Simple Approach without HF. *Chemistry A European J* **2017**, *23* (50), 12092–12095. https://doi.org/10.1002/chem.201702375.
(28) Wu, C.; Lu, X.; Peng, L.; Xu, K.; Peng, X.; Huang, J.; Yu, G.; Xie, Y. Two-Dimensional Vanadyl Phosphate Ultrathin Nanosheets for High Energy Density and Flexible Pseudocapacitors. *Nat Commun* **2013**, *4* (1), 2431. https://doi.org/10.1038/ncomms3431.
(29) Bianchini, M.; Brisset, N.; Fauth, F.; Weill, F.; Elkaim, E.; Suard, E.; Masquelier, C.; Croguennec, L. $Na_3V_2(PO_4)_2F_3$ Revisited: A High-Resolution Diffraction Study. *Chem. Mater.* **2014**, *26* (14), 4238–4247. https://doi.org/10.1021/cm501644g.
(30) Olchowka, J.; Tailliez, T.; Bourgeois, L.; Dourges, M. A.; Guerlou-Demourgues, L. Ionic Liquids to Monitor the Nano-Structuration and the Surface Functionalization of Material Electrodes: A Proof of Concept Applied to Cobalt Oxyhydroxide. *Nanoscale Adv.* **2019**, *1* (6), 2240–2249. https://doi.org/10.1039/C9NA00171A.
(31) Boahen, E. K.; Pan, B.; Kweon, H.; Kim, J. S.; Choi, H.; Kong, Z.; Kim, D. J.; Zhu, J.; Ying, W. B.; Lee, K. J.; Kim, D. H. Ultrafast, Autonomous Self-Healable Iontronic Skin Exhibiting Piezo-Ionic Dynamics. *Nat Commun* **2022**, *13* (1), 7699. https://doi.org/10.1038/s41467-022-35434-8.

(32) Madheswaran, D. K.; Thangamuthu, M.; Krishna, R.; Gopi, S.; Geo Varuvel, E. Enhanced Oxidation Resistance and Electrochemical Performance of PEMFC Gas Diffusion Layer through [EMIM][TFSI] Ionic Liquid Coating. *Renewable Energy* **2024**, *235*, 121303. https://doi.org/10.1016/j.renene.2024.121303.
(33) Olchowka, J.; Invernizzi, R.; Lemoine, A.; Allouche, J.; Baraille, I.; Flahaut, D.; Guerlou-Demourgues, L. Stabilization and Improvement of Energy Storage Performance of High Mass Loading Cobalt Hydroxide Electrode by Surface Functionalization. *J. Electrochem. Soc.* **2020**, *167* (10), 100527. https://doi.org/10.1149/1945-7111/ab9a03.
(34) Cho, J.; Park, B. Preparation and Electrochemical/Thermal Properties of $LiNi_{0.74}Co_{0.26}O_2$ Cathode Material. *Journal of Power Sources* **2001**, *92* (1–2), 35–39. https://doi.org/10.1016/S0378-7753(00)00499-7.
(35) Sinha, N. N.; Munichandraiah, N. The Effect of Particle Size on Performance of Cathode Materials of Li-Ion Batteries *Journal of the Indian Institute of Science*. **2009**, *89*. 381
(36) Chi, Z.-X.; Zhang, W.; Cheng, F.-Q.; Chen, J.-T.; Cao, A.-M.; Wan, L.-J. Optimizing the Carbon Coating on $LiFePO_4$ for Improved Battery Performance. *RSC Adv.* **2014**, *4* (15), 7795. https://doi.org/10.1039/c3ra47702a.
(37) Chen, Z.; Zhang, Q.; Liang, Q. Carbon-Coatings Improve Performance of Li-Ion Battery. *Nanomaterials* **2022**, *12* (11), 1936. https://doi.org/10.3390/nano12111936.
(38) Meng, Y.; Xia, J.; Wang, L.; Wang, G.; Zhu, F.; Zhang, Y. A Comparative Study on $LiFePO_4$/C by in-Situ Coating with Different Carbon Sources for High-Performance Lithium Batteries. *Electrochimica Acta* **2018**, *261*, 96–103. https://doi.org/10.1016/j.electacta.2017.12.127.
(39) Wang, Y.; Liu, Z.; Zhou, S. An Effective Method for Preparing Uniform Carbon Coated Nano-Sized $LiFePO_4$ Particles. *Electrochimica Acta* **2011**, *58*, 359–363. https://doi.org/10.1016/j.electacta.2011.09.053.
(40) Zhang, X.; Kühnel, R.-S.; Hu, H.; Eder, D.; Balducci, A. Going Nano with Protic Ionic Liquids—the Synthesis of Carbon Coated $Li_3V_2(PO_4)_3$ Nanoparticles Encapsulated in a Carbon Matrix for High Power Lithium-Ion Batteries. *Nano Energy* **2015**, *12*, 207–214. https://doi.org/10.1016/j.nanoen.2014.12.008.
(41) Zhao, L.; Hu, Y.; Li, H.; Wang, Z.; Chen, L. Porous $Li_4Ti_5O_{12}$ Coated with N-Doped Carbon from Ionic Liquids for Li-Ion Batteries. *Advanced Materials* **2011**, *23* (11), 1385–1388. https://doi.org/10.1002/adma.201003294.
(42) Maccario, M.; Croguennec, L.; Desbat, B.; Couzi, M.; Cras, F. L.; Servant, L. Raman and FTIR Spectroscopy Investigations of Carbon-Coated Li_xFePO_4 Materials. *Journal of The Electrochemical Society*.2008, 155, A879. https://doi.org/10.1149/1.2977961
(43) Beattie, D. A.; Arcifa, A.; Delcheva, I.; Le Cerf, B. A.; MacWilliams, S. V.; Rossi, A.; Krasowska, M. Adsorption of Ionic Liquids onto Silver Studied by XPS. *Colloids and Surfaces A: Physicochemical and Engineering Aspects* **2018**, *544*, 78–85. https://doi.org/10.1016/j.colsurfa.2018.02.007.
(44) Xue, Gi.; Dai, Quinpin.; Jiang, Shuangen. Chemical Reactions of Imidazole with Metallic Silver Studied by the Use of SERS and XPS Techniques. *J. Am. Chem. Soc.* **1988**, *110* (8), 2393–2395. https://doi.org/10.1021/ja00216a009.
(45) Weingarth, D.; Foelske-Schmitz, A.; Wokaun, A.; Kötz, R. In Situ Electrochemical XPS Study of the Pt/[EMIM][BF_4] System. *Electrochemistry Communications* **2011**, *13* (6), 619–622. https://doi.org/10.1016/j.elecom.2011.03.027.
(46) Shen, W.; Wang, C.; Xu, Q.; Liu, H.; Wang, Y. Nitrogen-Doping-Induced Defects of a Carbon Coating Layer Facilitate Na-Storage in Electrode Materials. *Advanced Energy Materials* **2015**, *5* (1), 1400982. https://doi.org/10.1002/aenm.201400982.
(47) Xu, Y.; Zhang, C.; Zhou, M.; Fu, Q.; Zhao, C.; Wu, M.; Lei, Y. Highly Nitrogen Doped Carbon Nanofibers with Superior Rate Capability and Cyclability for Potassium Ion Batteries. *Nat Commun* **2018**, *9* (1), 1720. https://doi.org/10.1038/s41467-018-04190-z.
(48) Dedryvère, R.; Maccario, M.; Croguennec, L.; Le Cras, F.; Delmas, C.; Gonbeau, D. X-Ray Photoelectron Spectroscopy Investigations of Carbon-Coated $Li_x FePO_4$ Materials. *Chem. Mater.* **2008**, *20* (22), 7164–7170. https://doi.org/10.1021/cm801995p.
(49) Broux, T.; Bamine, T.; Fauth, F.; Simonelli, L.; Olszewski, W.; Marini, C.; Ménétrier, M.; Carlier, D.; Masquelier, C.; Croguennec, L. Strong Impact of the Oxygen Content in $Na_3V_2(PO_4)_2F_{3-y}O_y$

($0 \leq y \leq 0.5$) on Its Structural and Electrochemical Properties. *Chem. Mater.* **2016**, *28* (21), 7683–7692. https://doi.org/10.1021/acs.chemmater.6b02659.
(50) Angell, C. A.; Sichina, W. J.; Oguni, M. Heat Capacity of Water at Extremes of Supercooling and Superheating. *J. Phys. Chem.* **1982**, *86* (6), 998–1002. https://doi.org/10.1021/j100395a032.
(51) Miyazawa, T.; Kondo, S.; Suzuki, T.; Sato, H. Specific Heat Capacity at Constant Pressure of Ethanol by Flow Calorimetry. *J. Chem. Eng. Data* **2012**, *57* (6), 1700–1707. https://doi.org/10.1021/je2013473.
(52) Dai, Z.; Chen, Y.; Liu, C.; Lu, X.; Liu, Y.; Ji, X. Prediction and Verification of Heat Capacities for Pure Ionic Liquids. *Chinese Journal of Chemical Engineering* **2021**, *31*, 169–176. https://doi.org/10.1016/j.cjche.2020.10.040.
(53) Sanmamed, Y. A.; Navia, P.; González-Salgado, D.; Troncoso, J.; Romaní, L. Pressure and Temperature Dependence of Isobaric Heat Capacity for [Emim][BF_4], [Bmim][BF_4], [Hmim][BF_4], and [Omim][BF_4]. *J. Chem. Eng. Data* **2010**, *55* (2), 600–604. https://doi.org/10.1021/je9004992.

Table of Content